Dynamic phase-driven cascade focusing and acceleration of subrelativistic electrons in on-chip inverse-Cherenkov particle accelerators

Minghao Liu and Weihao Liu*

College of Electronic and Information Engineering, Nanjing University of Aeronautics and Astronautics, Nanjing, Jiangsu, 211106, China
and Key Laboratory of Radar Imaging and Microwave Photonics (Nanjing University of Aeronautics and Astronautics), Ministry of Education, Nanjing, China

Liwen Zhang

Institute of Advanced Science Facilities, Shenzhen, 518107, China

Shengguang Liu

Key Laboratory for Laser Plasmas (Ministry of Education), Shanghai Jiao Tong University, Shanghai 200240, China

(Received 21 October 2024; accepted 9 July 2026; published 11 August 2026)

The inverse-Cherenkov dielectric laser accelerator (ICR-DLA) holds great promise as a compact, on-chip accelerator for a wide range of future applications. However, two significant challenges—bunch dispersion/deflection and phase slippage—have hindered its development in the subrelativistic regime. In this paper, we propose an approach that addresses both issues simultaneously by utilizing a single laser pulse to illuminate a staged dielectric prism. Our method leverages the phase slippage experienced by subrelativistic electrons during high-gradient acceleration, allowing these electrons to encounter alternating focusing and defocusing forces throughout the acceleration process. This technique enables stable, long-range bunch transport within a miniaturized acceleration channel. We show that cascading focusing and acceleration of subrelativistic electrons can be achieved in a multistage acceleration structure, laying a foundation to bridge the gap between subrelativistic and relativistic regimes, which is crucial for the realization of a practical on-chip particle accelerator.

DOI: 10.1103/d2ff-sq6k

I. INTRODUCTION

Particle accelerators play a crucial role in fundamental physics research [1,2], medical applications [3–5], and various industrial activities [6–8]. However, conventional radio-frequency (rf) accelerators face significant limitations as the demand for higher energy and more compact designs continues to grow [9–11]. Their large dimensions, high costs, and low breakdown thresholds restrict their broader applicability, particularly in scenarios requiring portable or tabletop setups. Accelerators based on the inverse-Cherenkov effect in gas and high-power microwaves [12–14] also encounter these limitations.

In response to these challenges, dielectric laser-driven accelerators (DLAs) have emerged as a promising alternative. DLAs offer notable advantages [15,16], including the potential for much larger acceleration gradients, reduced size, and lower costs than traditional rf accelerators. These advantages stem from the superior breakdown thresholds of dielectric materials compared to metals, the feasibility of using commercially available high-power lasers, and the potential for on-chip integration [17], leading to highly compact accelerator designs. Additionally, the utilization of optical frequencies allows for precise control and manipulation of accelerating fields over extremely short timescales. The DLAs based on the inverse Smith-Purcell (ISP-DLA) [18,19] and inverse-Cherenkov (ICR-DLA) [20–23] effects have garnered significant attention in recent years as key classes of on-chip particle accelerators. ICR-DLA and ISP-DLA employ different mechanisms for electron acceleration, each with inherent advantages and limitations. In ISP-DLA, electrons are accelerated via discrete space harmonics within a periodic structure. Although this method has a low acceleration efficiency relative to ICR-DLA, it provides greater flexibility in structural design and scalability. To optimize the interaction length,

*Contact author: liuwhao@nuaa.edu.cn

ISP-DLA often incorporates pulse front tilting (PFT) and extended pulse durations, which introduce additional complexity. In contrast, ICR-DLA utilizes evanescent fields produced by total internal reflection in the dielectric prism, enabling high acceleration efficiency without the need for pulse front manipulation. However, this approach is constrained by the dielectric refractive index due to the requirement of ICR acceleration.

However, a primary challenge in practically implementing DLAs lies in effectively bridging the gap between subrelativistic and relativistic particle acceleration [24,25]. Accelerating subrelativistic particles efficiently presents difficulties due to phase slippage [26], which occurs as these particles experience significant velocity changes during acceleration, ultimately leading to reduced efficiency. Furthermore, the space charge effect becomes pronounced in the subrelativistic regime, causing particle bunches to disperse or deflect, which diminishes the transmission efficiency of the electron bunch. These issues are particularly pronounced in DLAs due to their microscale architectures and the reliance on short-wavelength operations [27,28].

For now, the alternative phase focusing (APF) method has been used to focus and accelerate the electron bunch, which was proposed and validated in ISP-DLA schemes [29–33] and the ICR-DLA scheme [34]. In the APF, the phase experienced by a particle jumps alternately in each focusing cell, and the phase experienced by a particle within a section should be kept unchanged, so a tapered prism with a curved surface has to be used to keep synchronization in each section, which poses a challenge for fabrication.

In this paper, we propose a cascaded dynamic phase-driven approach that addresses both accelerating and confining the bunch simultaneously for long-acceleration-range ICR-DLA. In contrast to the APF scheme, the phase velocity of the acceleration wave in our approach does not necessarily match the particle velocity. This tolerance relaxes the nanoscale fabrication requirements and improves the practical feasibility. Moreover, the absence of phase jumps during acceleration ensures smoother focusing dynamics. The present method utilizes phase slippage (mismatching) in subrelativistic electrons under high-gradient acceleration, which causes them to continuously alternate focusing and defocusing throughout acceleration. This facilitates stable long-range bunch transport within a miniaturized acceleration channel, which is essential for the development of a practical on-chip particle accelerator.

II. MODEL DESCRIPTION

The proposed scheme, illustrated in Fig. 1, employs a pair of P-polarization lasers to illuminate a four-stage tapered prism via the ICR effect [35]. The lasers, incident on the side surface of the prism, are refracted with taper angles ($\alpha_1 > \alpha_2 > \alpha_3 > \alpha_4$), exciting the acceleration field

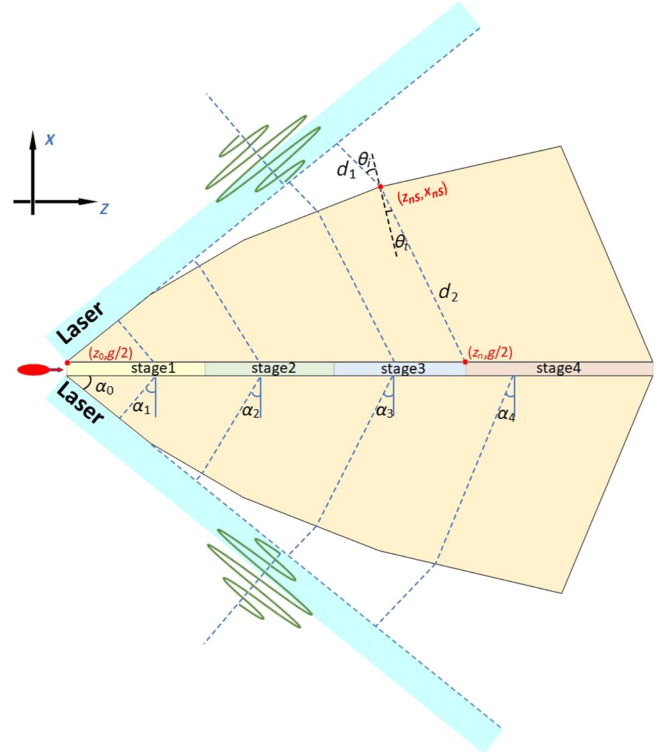

FIG. 1. Schematic of the proposed cascade dielectric laser accelerator.

through total internal reflection at the boundary of the bunch channel. The phase velocity of the acceleration field, given by $v_{p_i} = \frac{c}{n \sin \alpha_i}$ (where c is the speed of light in a vacuum, n is the refractive index, and i indicates 1, 2, 3, …), increases with each stage, intentionally exceeding the particle's initial velocity but remaining below its exit velocity; that is, the particles are kept in dynamic synchronization with the acceleration wave. This dynamic synchronization results in the particle alternating between lateral divergence and convergence phases during acceleration, allowing stable beam transport and optimizing the pass ratio.

As we consider that the electric field in the y axis is uniform, we ignore the y variation in the field expression. The field expressions in the upper prism and the bunch channel are as follows:

$$\begin{aligned} E_z &= \eta_1 \cos\alpha [H_{im} \exp(-jk_{x1}x) - H_{rm} \exp(jk_{x1}x)] \exp(j\phi) \\ E_x &= \eta_1 \sin\alpha [H_{im} \exp(-jk_{x1}x) + H_{rm} \exp(jk_{x1}x)] \exp(j\phi) \,, \\ H_y &= [H_{im} \exp(-jk_{x1}x) + H_{rm} \exp(jk_{x1}x)] \exp(j\phi) \end{aligned} \quad (1)$$

$$\begin{aligned} E_z &= E_m \cosh(-jk_x x) \exp(j\phi) \\ E_x &= -jE_m \frac{k_z}{k_x} \sinh(-jk_x x) \exp(j\phi) \\ H_y &= -jE_m \frac{\omega \varepsilon_0}{k_x} \sinh(-jk_x x) \exp(j\phi) \end{aligned} \quad , \quad (2)$$

in which

$$\begin{aligned} \phi &= k_z z - \omega t + \phi_0 \\ E_m &= \frac{2k_x \eta_1 \cos \alpha n^2 \exp(-jk_{x1} g/2)}{k_{x1} \sinh(-jk_x g/2) + jn^2 k_x \cosh(-jk_x g/2)} H_{im}, \\ H_{im} &= \frac{2\eta_0 \cos \theta_i}{\eta_0 \cos \theta_i + \eta_1 \cos \theta_t} H_0 \end{aligned} \tag{3}$$

ω is the center angular frequency of the incident laser. k_z and k_x represent the longitudinal and transverse wavenumber of the acceleration wave in the bunch channel. $k_{x1} = k_1 \cos \alpha$, α represents the incident angle of the laser between the dielectric and bunch channel. n is the refractive index of the dielectric. η_0, η_1, and k_1 represent the wave impedance of the vacuum, the dielectric, and the wavenumber in the dielectric. Besides, g, θ_i, and θ_t represent the width of the bunch channel, the incident angle, and the refraction angle between the air and the prism, respectively.

The transverse and longitudinal forces exerted on the particles can be respectively expressed as follows:

$$\begin{aligned} F_x &= qE_x - q\mu v H_y \\ F_z &= qE_z \end{aligned}. \tag{4}$$

Next, the particle dynamic equation in the longitudinal direction reads

$$\frac{d\gamma}{dz} = q \frac{1}{m_0 c^2} |E_m| \cosh(-jk_x x) \cos(\varphi_z), \tag{5}$$

in which $\gamma = 1/\sqrt{1-\beta^2} = 1/\sqrt{1-(v_e/c)^2}$ is the Lorentz factor, q represents the charge quantity, and

$$\begin{aligned} \varphi_z &= \delta_\varphi(z) + \varphi + \arg(E_m) \\ \delta_\varphi(z) &= \int_0^z \left(\frac{\omega}{v_{pn}} - \frac{\omega}{v_e(z)} \right) dz \end{aligned}, \tag{6}$$

in which v_{pn} and v_e represent the velocity of the acceleration wave in each stage of the bunch channel and electron bunch. δ_φ represents the integrated phase difference between the acceleration wave and the electron bunch.

To ensure phase continuity across successive acceleration stages, the starting coordinates of the prism side surface in each stage, denoted as ($z_n s$ and $x_n s$), must be aligned in accordance with the following relation [36]:

$$\begin{cases} \Delta\phi(z_0) = \Delta\phi(z_n) + k_0 d_1 + k_1 d_2 - \omega \Delta_t \\ d_1 + d_2 \cos(\alpha_0 - \alpha_n) = (z_n - z_0) \sin \alpha_0 \end{cases}, \tag{7}$$

in which $\Delta\phi(z_n) = \arg(E_m) + k_1 \cos \alpha_n \frac{g}{2}$ and $\Delta_t = \int_{z_0}^{z_n} \frac{1}{v_e(z)} dz$.

Within each stage of the prism, the phase velocity of the acceleration wave is constant, and the phase experienced by the particles changes continuously. Thus, we can use Eqs. (5) and (6) to design the tapered angle and channel length in each stage of the prism according to the phase slippage situation of the particles, whereby the particles are not only always located in the acceleration phase but also switch controllably from the focused phase and the defocused phase. The designed phase curve is shown in Fig. 2. Besides, the acceleration stages of the prism can be further extended according to Eq. (6). For longer acceleration lengths, the structure can be subdivided into multiple prisms, each illuminated by a separate laser pulse, thereby effectively extending the interaction without requiring PFT.

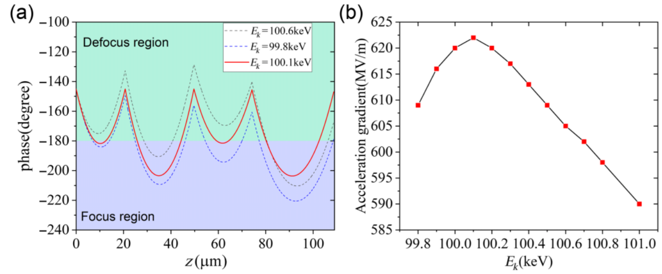

FIG. 2. (a) Theoretically designed phase experienced by the single particle versus the position of the particle at 99.8, 100.1, and 100.6 keV. (b) Theoretical acceleration gradient of the electron at the same emission phase versus the initial particle energy.

III. SIMULATION

In the simulation, we first employ the finite difference time domain method (FDTD) in Lumerical to obtain the frequency-domain field distribution within the bunch channel. We select silicon as the prism's dielectric material due to its high breakdown threshold, which can be fabricated by high aspect ratio etching [37]. The bunch channel is set with a length of 108.7 μm and a width of 0.3 μm. The stimulating laser follows a Gaussian temporal distribution with a FWHM of 160 fs, which decreases the possibility of an optical instrument being broken and increases the incidence of electric field intensity at the same damage threshold. The peak amplitude of the stimulating laser is set to 1 GV/m, and the central incident wavelength is set to 2 μm, following previous work [32]. The laser fluence on the prism's lateral surface is 0.016 $\mathrm{J/cm^2}$, well below the silicon structure's damage threshold observed in the experiment (0.19 $\mathrm{J/cm^2}$) [38]. The present amplitude of the stimulating laser may cause nonlinear effects. However, this can be mitigated by thinning each stage of the prism through the removal of dielectric material with a thickness corresponding to an integer multiple of the operating wavelength. We ignore the nonlinear effects here to simplify the simulation and illustrate the theory of the proposed scheme. In the simulation, the transverse size of the laser beam is

TABLE I. Simulation parameters.

Symbol	Physical quantity	Value
E_k	Initial centered particle energy	100.1 keV
ε	Initial rms transverse emittance	0.5 pm $\cdot$ rad
w_x	Bunch width in the x direction	60 nm
w_y	Bunch width in the y direction	600 nm
l_z	Longitudinal bunch length	0.04 μm
τ	Full width at half maximum (FWHM) laser pulse duration	160 fs
λ	Central wavelength of the laser	2 μm
E_0	Amplitude of the incident laser	1 GV/m
n	Refractive index	3.47
α_1, α_2, α_3, α_4	Incident angle	31°, 29.3°, 27.9°, 26.6°
g	Channel width	0.3 μm
L	Longitudinal length	108.7 μm

considered to exceed the side surface of the prism. The bunch with the specified characteristrics can be obtained by compressing the bunch to attosecond length by a dielectric structure mentioned in Ref. [39].

Furthermore, the amplitude of the electric field within the bunch channel and its inner face is lower than that at the incident surface, indicating that the fluence of the accelerating field in the bunch channel remains beneath the damage threshold of silicon. The simulated field distribution is then input into a 3D particle tracer code, General Particle Tracer (GPT), to simulate particle dynamics within the bunch channel. The initial centered electron energy is set to 100.1 keV, and the electron bunch also follows a Gaussian distribution in both transverse and longitudinal directions, with an initial emittance of 0.5 pm $\cdot$ rad in the x direction. In the particle tracking simulation, we ignore the space charge effect, which is consistent with the current subrelativistic DLA experiments [32], and set the number of macro particles to 2,000 to reduce statistical errors. The parameters used in the simulations are given in Table I. The particle energies corresponding to the phase velocity at each stage of the accelerating field are 106, 120.8, 137.5, and 156.5 keV, satisfying the requirement of dynamic synchronization.

Figure 2(a) shows the designed phase curve of a single particle under dynamic synchronization. By using the phase slippage of a subrelativistic particle, the particle transits alternately between the transverse defocusing region (with phase angle above $-180°$) and the focusing region (with phase angle below $-180°$) in the acceleration process. Hence, the particle bunch will be dynamically focused just as in conventional focusing and defocusing quadrupoles of an rf accelerator. Figure 2(b) shows the theoretical acceleration gradient of the electron emitted at $-145°$ versus its energy. We can see that the acceleration gradient decreases when the initial particle energy deviates from its designed value.

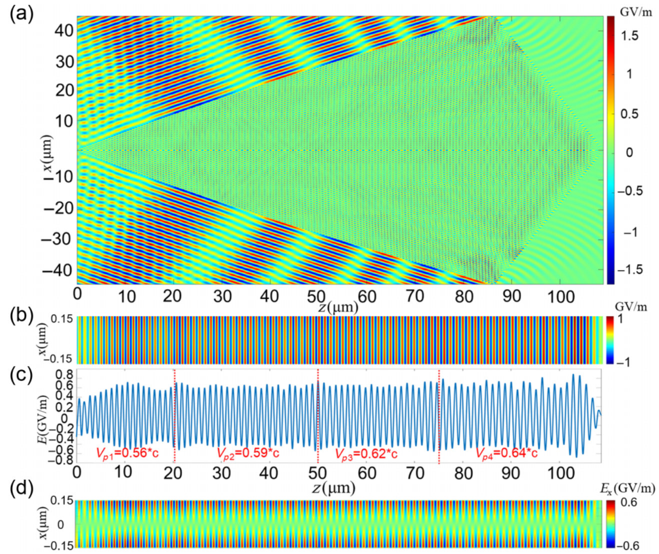

FIG. 3. Simulated real part of the longitudinal electric field of the whole prism (a), the bunch channel (b), the center of the channel (c), and the transverse electric field of the bunch channel (d).

Simulated frequency-domain electric field distributions of the proposed scheme are shown in Fig. 3. The simulated longitudinal electric field E_z exhibits a uniform distribution along the x axis, whereas the transverse component E_x intensifies near the channel surface. Figure 4 illustrates the simulated trapped phase space during acceleration, defined by particles maintaining an acceleration gradient above 610 MV/m while traversing the channel. As shown in Fig. 4(a), when the initial particle energy significantly exceeds the design value, the range of phases that can be stably captured narrows considerably. We can see that the present method does not rely on a fixed synchronous phase, unlike conventional APF designs. Figure 4(b) shows that the captured phase ranges vary with lateral position within the channel.

Then, we consider the dynamics of a bunch of electrons. Figure 5 shows the simulated dot density map of the simulated $x-\beta_x$ phase space and particle trajectories of

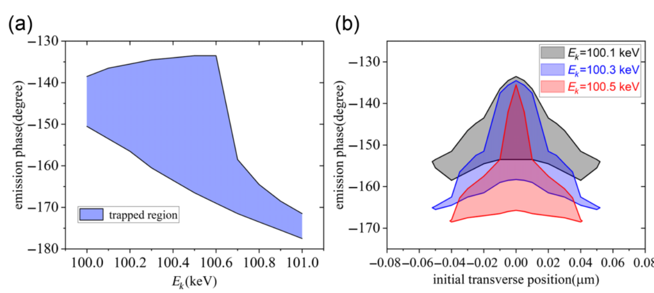

FIG. 4. (a) Simulated trapped emission phase versus initial particle energy of a single particle emitted at $x = 0$ μm. (b) Simulated trapped emission phase versus initial emission position (x) of a single particle at 100.1, 100.3, and 100.5 keV.

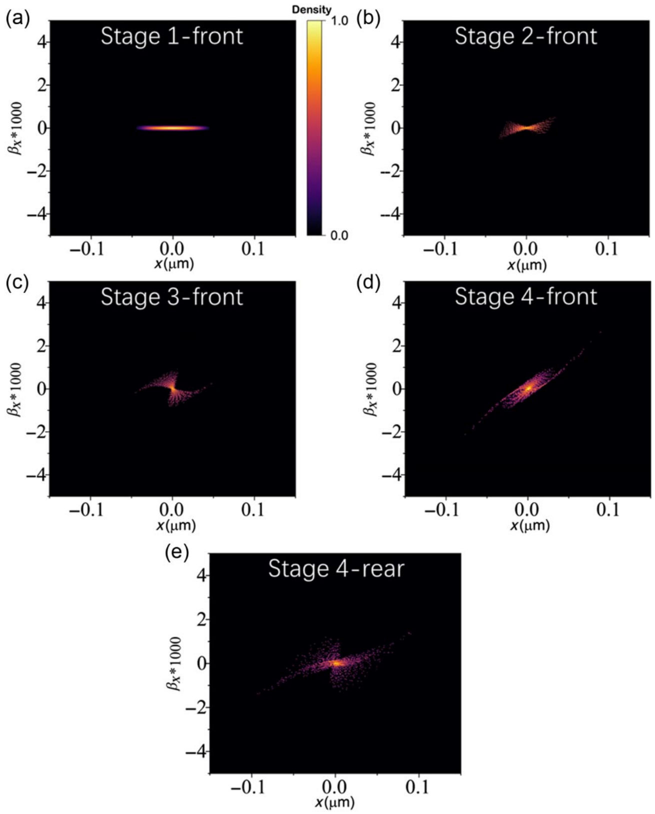

FIG. 5. (a)–(e) Simulated x-β_x phase space of the bunch in each stage.

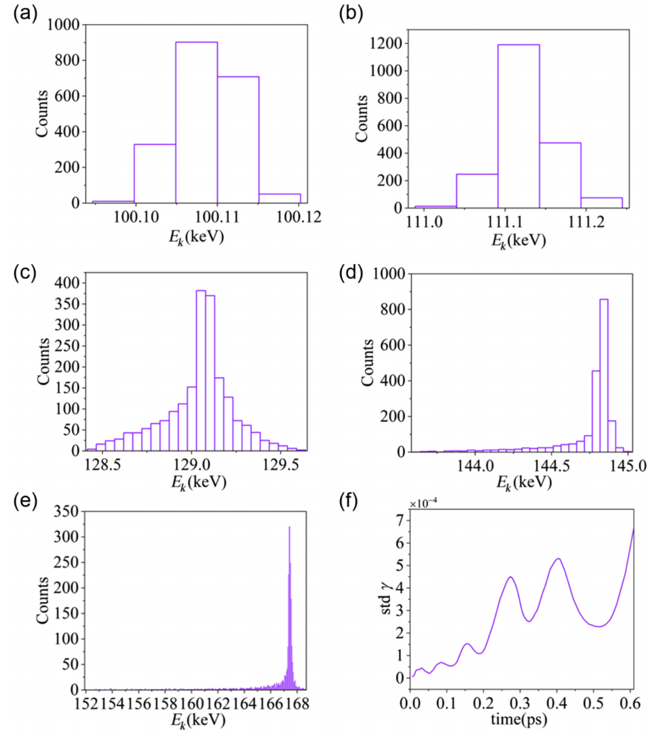

FIG. 7. Simulated particle energy distribution at $z = 0$ μm (a), $z = 20.7$ μm (b), $z = 49.7$ μm (c), $z = 74.2$ μm (d), $z = 108.7$ μm (e), and standard γ deviation of the matched bunch versus time (f).

the electron bunch in the bunch channel. We can see that the electron beam undergoes a process of alternative defocusing and focusing as expected throughout the entire bunch channel. As illustrated in Fig. 6, the transverse profile of the bunch undergoes two successive cycles of expansion followed by convergence, consistent with the theoretically predicted dynamics. Throughout this process, the beam remains well confined near the center of the channel, indicating stable transverse guidance.

Figures 7(a)–7(e) show the energy distributions of the electron bunch in the initial state and four stages. We can see that about 95% of the particles are accelerated to within the FWHM centered at an energy of 167 keV. As shown in Fig. 7(f), the energy spread of the accelerated bunch remains below 10^{-3} while oscillating periodically throughout the acceleration process. This is because all of the particles periodically experience transverse focusing and defocusing, which makes them experience varying acceleration fields in the transverse position.

The simulated pass ratio and average energy of the electron bunch relative to the longitudinal position are shown in Fig. 8, wherein the results of the initial synchronization case are shown for comparison. We can see that the pass ratio is 100% after 108.7 μm transport,

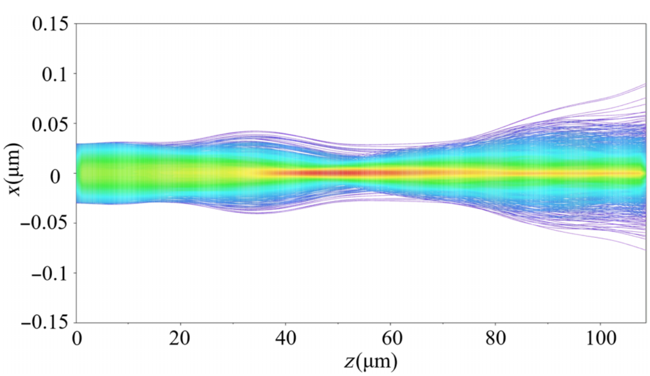

FIG. 6. Simulated density map of particle trajectories versus the particle position.

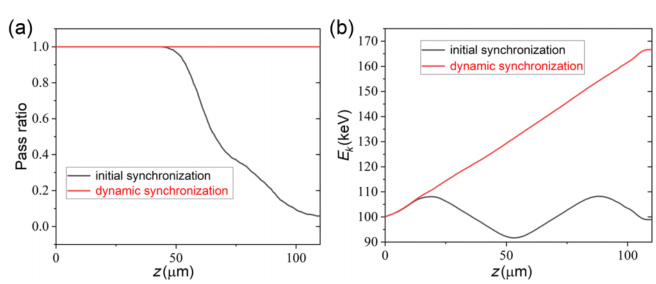

FIG. 8. (a) Simulated pass ratio versus the particle position. (b) Simulated average electron energy versus transmission length in dynamic and initial synchronization.

while it drops to nearly zero in the initial synchronization case. This confirms the effectiveness of the proposed dynamic synchronization method. Figure 8(b) shows that the average energy of the electron bunch increases steadily due to continuous acceleration in the case of dynamic synchronization. The average acceleration gradient is about 612 MV/m. In contrast, the acceleration length is greatly limited, and the energy gain fluctuates to zero in the case of initial synchronization due to phase slippage.

IV. CONCLUDES

In conclusion, we propose an inverse-Cherenkov dielectric laser accelerator using a dynamic synchronization method and incorporating a four-stage tapered construction to facilitate continuous acceleration while controlling the transverse divergence and convergence of particles. The electron bunch in the narrow channel under dynamic synchronization can be controlled, and continuous acceleration can be achieved for subrelativistic particles. Simulation results reveal that particles can be accelerated from 100.1 to 167 keV within a small 108.7-μm-long structure and provide the acceleration gradient of 612 MV/m. This scheme can afford a promising option for the tabletop ultrafast electron accelerator, greatly improving the accessibility and utility of particle acceleration technology across diverse domains.

ACKNOWLEDGMENTS

This work was supported by the Natural Science Foundation of China (Grant No. 12475153), the Key State Laboratory of Advanced Electromagnetic Technology (Grant No. AET 2025KF001), the Key National Laboratory of Electromagnetic On Environment Effects of Science and Technology (No. 6142205250201), and the Interdisciplinary Innovation Fund for Doctoral Students of Nanjing University of Aeronautics and Astronautics (Grant No. KXKCXJJ202609).

DATA AVAILABILITY

There are no publicly available research data or software supporting this manuscript. Requests for further information or data should be sent to the authors.

[1] S. V. Kutsaev, Advanced technologies for applied particle accelerators and examples of their use, Tech. Phys. **66**, 161 (2021).

[2] V. N. Starovoitova, L. Tchelidze, and D. P. Wells, Production of medical radioisotopes with linear accelerators, Appl. Radiat. Isotopes **85**, 39 (2014).

[3] W. P. Levin, H. Kooy, J. S. Loeffler, and T. F. DeLaney, Proton beam therapy, Br. J. Cancer **93**, 849 (2005).

[4] T. D. Malouff, A. Mahajan, S. Krishnan, C. Beltran, D. S. Seneviratne, and D. M. Trifiletti, Carbon ion ther apy: A modern review of an emerging technology, Front. Oncol. **10**, 82 (2020).

[5] J. S. Loeffler and M. Durante, Charged particle ther apy—optimization, challenges and future directions, Nat. Rev. Clin. Oncol. **10**, 411 (2013).

[6] K. Hossain, Y. A. Maruthi, N. L. Das, K. P. Rawat, and K. S. S. Sarma, Irradiation of wastewater with electron beam is a key to sustainable smart/green cities: A review, Appl. Water Sci. **8**, 1 (2018).

[7] P. A. Bystrov, Y. S. Pavlov, O. V. Souvorova, and I. Y. Yakupov, Formation of irradiation beams on accelera- tor UELV-10-10-70 for research of the radiation resistance of polymers, Radiat. Phys. Chem. **161**, 83 (2019).

[8] F. Lin, Y. Liu, X. Yu, L. Cheng, A. Singer, O. G. Shpyrko, H. L. Xin, N. Tamura, C. Tian, T.-C. Weng, X.-Q. Yang, Y. S. Meng, D. Nordlund, W. Yang, and M. M. Doeff, Synchrotron x-ray analytical techniques for studying materials electrochemistry in rechargeable batteries, Chem. Rev. **117**, 13123 (2017).

[9] T. P. Wangler, *RF Linear Accelerators* (John Wiley & Sons, New York, 2008).

[10] J. Rosenzweig and L. Serafini, Transverse particle motion in radio-frequency linear accelerators, Phys. Rev. E **49**, 1599 (1994).

[11] G. Ciovati, Effect of low-temperature baking on the radio-frequency properties of niobium superconducting cavities for particle accelerators, J. Appl. Phys. **96**, 1591 (2004).

[12] W. D. Kimura, G. H. Kim, R. D. Romea, L. C. Steinhauer, I. V. Pogorelsky, K. P. Kusche, R. C. Fernow, X. Wang, and Y. Liu, Laser acceleration of relativistic electrons using the inverse cherenkov effect, Phys. Rev. Lett. **74**, 546 (1995).

[13] T. B. Zhang and T. C. Marshall, A microwave inverse Cherenkov accelerator (MICA), Nucl. Instrum. Methods Phys. Res. Sect. A **375**, 614 (1996).

[14] K. Shimoda, Proposal for an electron accelerator using an optical maser, Appl. Opt. **1**, 33 (1962).

[15] E. A. Peralta, K. Soong, R. J. England, E. R. Colby, Z. Wu, B. Montazeri, C. McGuinness, J. McNeur, K. J. Leedle, D. Walz, E. B. Sozer, B. Cowan, B. Schwartz, G. Travish, and R. L. Byer, Demonstration of electron acceleration in a laser-driven dielectric microstructure, Nature (London) **503**, 91 (2013).

[16] J. Breuer and P. Hommelhoff, Laser-based acceleration of nonrelativistic electrons at a dielectric structure, Phys. Rev. Lett. **111**, 134803 (2013).

[17] U. Niedermayer, O. Boine-Frankenheim, and T. Egenolf, Designing a dielectric laser accelerator on a chip, in *Journal of Physics: Conference Series* (IOP Publishing, 2017), Vol. 874, p. 012041.

[18] J. Breuer and P. Hommelhoff, Dielectric laser accelera tion of 28 keV electrons with the inverse Smith–Purcell effect, Nucl. Instrum. Methods Phys. Res. Sect. A **740**, 114 (2014).

[19] N. Talebi, Schrödinger electrons interacting with optical gratings: Quantum mechanical study of the inverse Smith–Purcell effect, New J. Phys. **18**, 123006 (2016).

[20] W. Liu, Z. Yu, L. Sun, Y. Liu, Q. Jia, H. Xu, and B. Sun, Microscale laser-driven particle accelerator using the

inverse Cherenkov effect, Phys. Rev. Appl. **14**, 014018 (2020).

[21] W. Liu, L. Zhang, Y. Liu, Q. Jia, B. Sun, and H. Xu, Toward a laser-driven traveling-wave linac on a chip, Phys. Rev. Appl. **19**, 044066 (2023).

[22] W. Liu, Z. Yu, L. Sun, Y. Liu, Q. Jia, H. Xu, and B. Sun, Microscale laser-driven particle accelerator using the inverse Cherenkov effect, Phys. Rev. Appl. **14**, 014018 (2020).

[23] W. Liu, Z. Yu, L. Sun, Y. Liu, Q. Jia, H. Xu, and B. Sun, Microscale laser-driven particle accelerator using the inverse Cherenkov effect, Phys. Rev. Appl. **14**, 014018 (2020).

[24] A. Hanuka and L. Schächter, Operation regimes of a dielectric laser accelerator, Nucl. Instrum. Methods Phys. Res. Sect. A **888**, 147 (2018).

[25] A. Hanuka and L. Schächter, Optimized operation of dielectric laser accelerators: Single bunch, Phys. Rev. Accel. Beams **21**, 054001 (2018).

[26] J. Breuer, J. McNeur, and P. Hommelhoff, Dielectric laser acceleration of electrons in the vicinity of single and double grating structures—theory and simulations, J. Phys. B **47**, 234004 (2014).

[27] K. P. Wootton, Z. Wu, B. M. Cowan, A. Hanuka, I. V. Makasyuk, E. A. Peralta, K. Soong, R. L. Byer, and R. Joel England, Demonstration of acceleration of relativistic electrons at a dielectric microstructure using femtosecond laser pulses, Opt. Lett. **41**, 2696 (2016).

[28] J. Breuer and P. Hommelhoff, Laser-based acceleration of nonrelativistic electrons at a dielectric structure, Phys. Rev. Lett. **111**, 134803 (2013).

[29] U. Niedermayer, T. Egenolf, O. Boine-Frankenheim, and P. Hommelhoff, Alternating-phase focusing for dielectric laser acceleration, Phys. Rev. Lett. **121**, 214801 (2018).

[30] U. Niedermayer, T. Egenolf, and O. Boine-Frankenheim, Three dimensional alternating-phase focusing for dielectric-laser electron accelerators, Phys. Rev. Lett. **125**, 164801 (2020).

[31] P. Broaddus, T. Egenolf, D. S. Black, M. Murillo, C. Woodahl, Y. Miao, U. Niedermayer, R. L. Byer, K. J. Leedle, and O. Solgaard, Subrelativistic alternating phase focusing dielectric laser accelerators, Phys. Rev. Lett. **132**, 085001 (2024).

[32] T. Chlouba, R. Shiloh, S. Kraus, L. Brückner, J. Litzel, and P. Hommelhoff, Coherent nanophotonic electron accelerator, Nature (London) **622**, 476 (2023).

[33] R. Shiloh, J. Illmer, T. Chlouba, P. Yousefi, N. Schönenberger, U. Niedermayer, A. Mittelbach, and P. Hommelhoff, Electron phase-space control in photonic chip-based particle acceleration, Nature (London) **597**, 498 (2021).

[34] L. Zhang, H. Xu, and W. Liu, Inverse Cherenkov dielectric laser accelerator with alternating phase focusing for sub relativistic particles, Phys. Rev. Accel. Beams **27**, 110401 (2024).

[35] L. Zhang, W. Liu, Y. Liu, Q. Jia, B. Sun, H. Xu, and S. Liu, Inverse Cherenkov dielectric laser accelerator for ultra-relativistic particles, J. Phys. D **56**, 045103 (2022).

[36] L. Zhang, W. Liu, H. Xu, S. Liu, and Y. Lu, Synchronous acceleration of subrelativistic particles in an inverse-Cherenkov dielectric laser accelerator with tapered phase velocity, IEEE Trans. Plasma Sci. **51**, 3484 (2023).

[37] H. Miao, L. Chen, M. Mirzaeimoghri, R. Kasica, and H. Wen, Cryogenic etching of high aspect ratio 400-nm pitch silicon gratings, J. Microelectromech. Syst. **25**, 963 (2016).

[38] K. Soong, R. Byer, E. Colby, R. England, and E. Peralta, Laser damage threshold measurements of optical materials for direct laser accelerators, in *AIP Conference Proceedings* (American Institute of Physics, 2012), pp. 511–515.

[39] U. Niedermayer, D. S. Black, K. J. Leedle, Y. Miao, R. L. Byer, and O. Solgaard, Low-energy-spread attosecond bunching and coherent electron acceleration in dielectric nanostructures, Phys. Rev. Appl. **15**, L021002 (2021).